

# Deterministic generation of frequency-bin-encoded microwave photons

Jiaying Yang<sup>1,2,\*</sup>, Maryam Khanahmadi<sup>1</sup>, Ingrid Strandberg<sup>1</sup>, Akshay Gaikwad<sup>1</sup>, Claudia Castillo-Moreno<sup>1</sup>, Anton Frisk Kockum<sup>1</sup>, Muhammad Asad Ullah<sup>2</sup>, Göran Johansson<sup>1</sup>, Axel Martin Eriksson<sup>1</sup>, and Simone Gasparinetti<sup>1†</sup>

<sup>1</sup>*Department of Microtechnology and Nanoscience,  
Chalmers University of Technology, SE-412 96, Göteborg, Sweden*

<sup>2</sup>*Ericsson Research, Ericsson AB, SE-164 83, Stockholm, Sweden*

(Dated: October 31, 2024)

A distributed quantum computing network requires a quantum communication channel between spatially separated processing units. In superconducting circuits, such a channel can be implemented based on propagating microwave photons to encode and transfer quantum information between an emitter and a receiver. However, traveling microwave photons can be lost during the transmission, leading to the failure of information transfer. Heralding protocols can be used to detect such photon losses. In this work, we propose such a protocol and experimentally demonstrate a frequency-bin encoding method of microwave photonic modes using superconducting circuits. We deterministically encode the quantum information from a superconducting qubit by simultaneously emitting its information into two photonic modes at different frequencies, with a process fidelity of 90.4%. The frequency-bin-encoded photonic modes can be used, at the receiver processor, to detect the occurrence of photon loss. Our work thus provides a reliable method to implement high-fidelity quantum state transfer in a distributed quantum computing network, incorporating error detection to enhance performance and accuracy.

*Introduction.*— Distributed quantum computing architectures, which allow multiple quantum processors to collaborate on larger tasks, offer a promising approach to improving the scalability of quantum computation [1, 2]. Implementing these architectures requires establishing quantum channels between remote quantum processors. For trapped-ion qubits [3], neutral atoms [4, 5], semiconductor quantum dots [6, 7], and color-center qubits [8, 9], quantum channels can be implemented using optical fibers to transmit photons over long distances. For superconducting circuits, quantum channels at microwave frequencies have been created using standing modes [10, 11] or traveling microwave photons [12–17], with the latter enabling a photon carrying quantum information to be emitted by the sender processor, travel through the quantum channel, and be reabsorbed by the receiver processor. This process enables deterministic quantum state transfer and remote entanglement between the qubits on both processors.

However, the emitted microwave photons are exposed to noise during the transmission in the quantum channel, posing a risk of photon loss or other signal corruption when transmitting quantum information between remotely distributed quantum processors. Heralding protocols for error detection can eliminate this issue by introducing an additional degree of freedom into the emission, such as time-bin [18, 19], frequency-bin [20–22], polarization [23], path [24, 25], or angular-momentum encoding [26], which are commonly used in the optical regime. In the microwave regime, time-bin-encoded photons have been experimentally demonstrated using superconducting qubits [27–29]. By emitting photons at different fre-

quencies simultaneously, frequency-bin encoding offers a higher data rate, effectively doubling the transmission speed compared to time-bin encoding using the same device. However, to the best of our knowledge, no implementation of the frequency-bin-encoded photon exists in the microwave regime. Furthermore, if such an implementation were to be developed, it would typically require additional hardware resources, such as extra qubits functioning as quantum state emitters, to emit both photonic modes simultaneously.

In this Letter, we propose and experimentally demonstrate frequency-bin-encoded photon generation, utilizing superconducting qubits in a waveguide quantum electrodynamics setup. The transmitted quantum information is encoded into a pair of simultaneously emitted propagating temporal modes at different frequencies, rather than between the vacuum state and the Fock state  $|1\rangle$ . The fact that the vacuum is not a logical state allows the frequency-bin-encoded photon to serve as a heralding protocol for error detection, addressing photon loss at the receiver processor. Our implementation is based on a qubit-coupler-qubit configuration [30–32]. However, instead of using the coupler to mediate qubit interactions, we tune the coupler into resonance with the emitter qubit, forming a hybridized emitter. By applying simultaneous excitation-preserving and non-preserving control pulses, we transfer the quantum state to the hybridized emitter and generate frequency-bin-encoded photons. This approach is hardware-efficient, eliminating the need for an additional emitter qubit coupled to the waveguide. We perform joint quantum state tomography on the frequency-bin modes, demonstrating encoding of qubit information into the frequency bins with an average state fidelity of 86.2% and a process fidelity of 90.4% in this first, proof-of-principle realization. Our device can serve as a building block in distributed

\* [jiyang@chalmers.se](mailto:jiyang@chalmers.se)

† [simoneg@chalmers.se](mailto:simoneg@chalmers.se); <https://202q-lab.se>

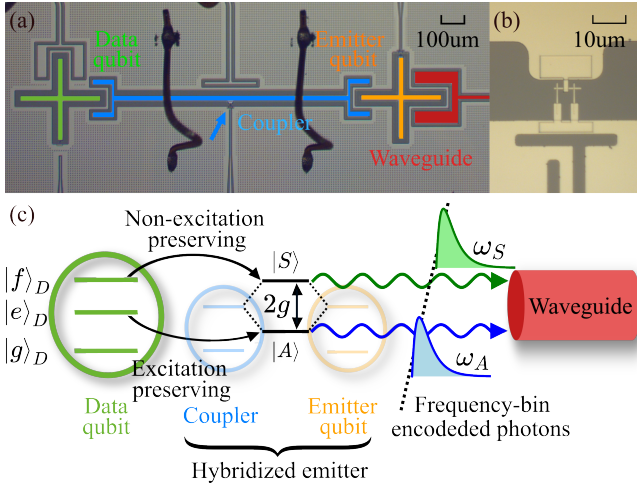


FIG. 1. Experimental implementation of frequency-bin-encoded photon generation based on a superconducting circuit. (a) False-color optical micrograph of the device, which consists of a data qubit (green), an emitter qubit (orange), a flux-tunable coupler (blue), and a waveguide (red). We wire-bond airbridges (black) across the top and bottom of the coupler to ensure a continuous and consistent ground connection. (b) Enlarged view of the superconducting quantum interference device (SQUID) of the coupler, whose position is indicated by the blue arrow in (a). (c) Schematic representation of the device for generation of frequency-bin photonic modes. The two modes are emitted at different frequencies  $\omega_A$  (blue) and  $\omega_S$  (green) simultaneously.

quantum computing systems, functioning as either an emitter or a receiver.

*Experimental setup.*— Our device is a superconducting quantum circuit comprising two X-mon-type [33] transmon qubits [34]—a data qubit (D) and an emitter qubit (E)—capacitively coupled via a parametric coupler [35] [Fig. 1(a)]. Qubit D has a transition frequency of  $\omega_D^{ge}/2\pi = 5.05$  GHz between its ground state  $|g\rangle$  and first excited state  $|e\rangle$ . The anharmonicity of qubit D is  $\alpha/2\pi = -215$  MHz. Both the coupler and qubit E are frequency-tunable by on-chip flux lines, enabled by superconducting quantum interference devices (SQUIDs). Their maximum frequencies are  $\omega_{C,0}/2\pi = 8.46$  GHz and  $\omega_{E,0}/2\pi = 6.17$  GHz, respectively, at zero magnetic flux. Qubit E is capacitively coupled to a coplanar waveguide with a decay rate of  $\Gamma_E/2\pi = 8$  MHz. Qubit D and the coupler are also capacitively coupled to one  $\lambda/4$  coplanar waveguide resonator each for characterization and readout. A summary of measured circuit parameters is available in the Supplementary Material (SM) [36] Sec. I.

*Hybridized emitter coupled to the waveguide.*— We generate frequency-bin-encoded photonic modes by simultaneously emitting two modes at distinct frequencies using the arrangement shown in Fig. 1(c). With a parametric coupler connected to Qubit E, and Qubit E being the only qubit physically coupled to the waveguide, we tune the coupler and Qubit E into resonance. The resonance between the coupler and Qubit E results in a hybridized

emitter with two modes [37, 38], a symmetric state  $|S\rangle = (|g\rangle_C |e\rangle_E + |e\rangle_C |g\rangle_E)/\sqrt{2}$  at  $\omega_S/2\pi = 5.79$  GHz and an antisymmetric state  $|A\rangle = (|g\rangle_C |e\rangle_E - |e\rangle_C |g\rangle_E)/\sqrt{2}$  at  $\omega_A/2\pi = 5.70$  GHz, where  $|g, e\rangle_{C(E)}$  define the bare states of the coupler (Qubit E) in a single-excitation manifold. The splitting between the two hybridized modes is  $(\omega_S - \omega_A)/2\pi = 2g/2\pi = 92$  MHz, with  $g$  the coupling rate between the coupler and Qubit E. These hybridized modes are coupled with the same strength to the waveguide, enabling simultaneous emission without requiring an additional degree of freedom, which leads to hardware-efficient operation. We apply an excitation-preserving parametric drive [30, 32, 35] through the coupler to transfer the first excited state of Qubit D to the antisymmetric mode, and a non-excitation-preserving second-order-transition drive [13, 27, 28, 39] through the charge line on qubit D, to transfer the second excited state of Qubit D to the symmetric mode. Thus, the hybridized emitter can be utilized as a source to emit two distinct propagating modes at their respective frequencies.

To characterize the population transfer to the hybridized emitter, we perform two measurements with varying drive strengths and frequencies of the parametric and second-order-transition drives. First, with Qubit D initialized in state  $|e\rangle_D$ , we measure its population while sweeping the parametric drive frequency  $\omega_{\text{param}}$ . When the frequency matches the resonance conditions  $\omega_A - \omega_D^{ge}$  or  $\omega_S - \omega_D^{ge}$ , the population transfers to the hybridized modes, reducing the population in  $|e\rangle_D$  [Fig. 2(a)]. The population dips become deeper and broader as the parametric-drive amplitude increases. In the second measurement, with Qubit D initialized in  $|f\rangle_D$ , we sweep the second-order drive frequency  $\omega_{2\text{nd}}$ . Resonant frequencies  $\omega_{2\text{nd}} = \omega_D^{ge} + \omega_D^{ef} - \omega_S$  and  $\omega_{2\text{nd}} = \omega_D^{ge} + \omega_D^{ef} - \omega_A$  result in dips in the population of  $|f\rangle_D$  [Fig. 2(b)], indicating the transfer of excitation to the waveguide via the hybridized modes. The frequency shift of the hybridized modes, induced by the parametric drive and the nonlinear relation between the coupler frequency and the DC flux [35, 40], is small, as evidenced by the near-constant dip frequencies despite increasing pulse amplitude [Fig. 2(b)]. In contrast, the AC Stark shift from the second-order drive [13] is significantly larger, as seen by the spectroscopy dips shifting to the left with increasing amplitude [Fig. 2(c)], which needs to be considered in the following experiments.

*Generation of frequency-bin-encoded photon.*— The frequency-bin-encoded photon is generated by simultaneously driving the transitions  $|e\rangle_D \rightarrow |A\rangle$  and  $|f\rangle_D \rightarrow |S\rangle$  using the parametric and second-order drives, respectively [Fig. 3(a)]. We start by initializing Qubit D in an arbitrary superposition state of the ground and first excited states,  $\alpha |g\rangle_D + \beta |e\rangle_D$ . Next,  $\pi_{ef}$  and  $\pi_{ge}$  pulses transform this state into the same superposition between the first and second excited states,  $\alpha |e\rangle_D + \beta |f\rangle_D$ . Subsequently, we simultaneously apply the parametric and second-order-transition drives. Due to the Stark-shift

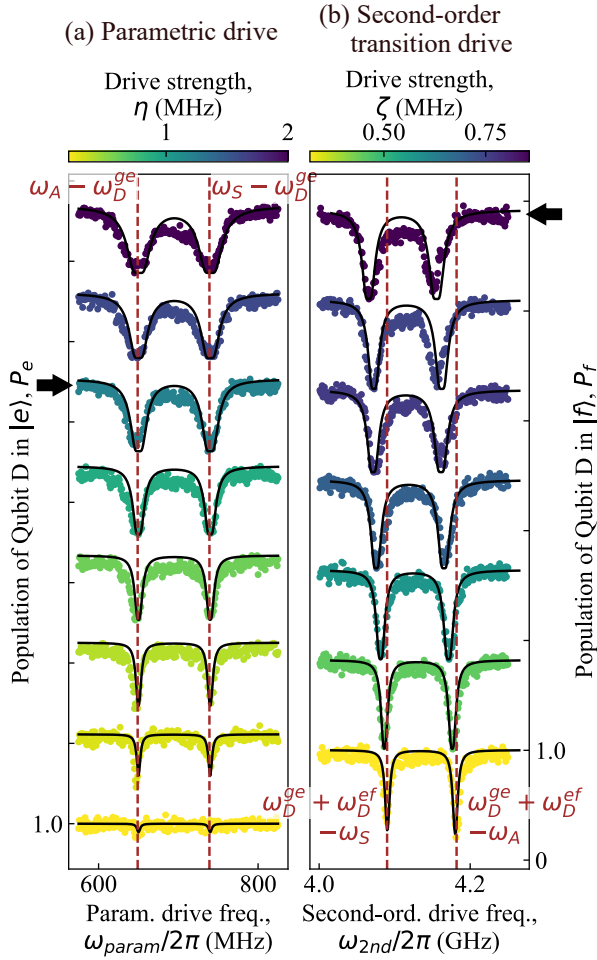


FIG. 2. Characterization of the hybridized modes. (a) The population of Qubit D in state  $|e\rangle_D$ , while sweeping the frequency and amplitude of the parametric drive. The filled circles represent the measured data and the solid black curve is the fitting from numerical simulation. Each curve is offset by 0.55 compared to the curve below it. (b) The population of Qubit D in state  $|f\rangle_D$ , while sweeping the frequency and amplitude of the second-order-transition drive. The filled circles represent the measured data and the solid black curve is the fitting from numerical simulation. Each curve is offset by 0.82 compared to the curve below it. The curves corresponding to the drive strengths used in subsequent experiments are highlighted with black arrows.

frequency  $\omega_{AC}$  from the second-order drive, we fix the frequency of the parametric drive and the second-order transition as  $\omega_{\text{param}} + \omega_{AC}$  and  $\omega_{2\text{nd}} + 2\omega_{AC}$ , which transfers the population to the  $|A\rangle$  and  $|S\rangle$  states of the hybridized emitter, respectively.

In a rotating frame defined by the Hamiltonian  $H_0 = \omega_D^{ge} \hat{d}^\dagger \hat{d} + \omega_A \hat{a}_A^\dagger \hat{a}_A + \omega_S \hat{a}_S^\dagger \hat{a}_S$ , the driven system is described by the effective Hamiltonian

$$H_{\text{eff}} = (\eta \hat{d}^\dagger \hat{a}_A + \eta^* \hat{d} \hat{a}_A^\dagger) + (\zeta \hat{d}^{\dagger 2} \hat{a}_S + \zeta^* \hat{d}^2 \hat{a}_S^\dagger) + \frac{\alpha}{2} \hat{d}^{\dagger 2} \hat{d}^2, \quad (1)$$

where the ladder operators  $\{(\hat{d}, \hat{d}^\dagger), (\hat{a}_A, \hat{a}_A^\dagger), (\hat{a}_S, \hat{a}_S^\dagger)\}$  describe the mode of Qubit D, the symmetric mode, and the antisymmetric mode, respectively (see SM [36] Sec. II for the full Hamiltonian). We do not consider the higher excited states of the coupler and Qubit E since they are barely occupied due to the anharmonicity. The drive strengths of the parametric drive ( $\eta$ ) and the second-order transition ( $\zeta$ ) should satisfy the relation  $\eta = \sqrt{2}\zeta$ , to ensure approximately equal emission rates from Qubit D to the two propagating modes, as the two drives correspond to one-photon and two-photon transitions, respectively. In our case, the strengths are chosen to be  $|\eta|/2\pi = 1.1$  MHz and  $|\zeta|/2\pi = 0.78$  MHz for subsequent experiments. Applying the simultaneous parametric and second-order drives transfers the state of Qubit D to the hybridized emitter state  $\alpha|A\rangle + \beta|S\rangle$ . Due to the hybridized emitter's large decay rate into the ground state,  $\Gamma \gg \eta, \zeta$ , it immediately decays to the ground state, emitting the entangled propagating modes  $\alpha|1\rangle_{\omega_A}|0\rangle_{\omega_S} + \beta|0\rangle_{\omega_A}|1\rangle_{\omega_S}$  into the waveguide, where  $i$  and  $j$  in  $|i\rangle_{\omega_A}|j\rangle_{\omega_S}$  denote the photon numbers at frequencies  $\omega_A$  and  $\omega_S$ , respectively.

It is worth noting that the reduced density matrix for each frequency mode obtained from the quantum state  $\alpha|1\rangle_{\omega_A}|0\rangle_{\omega_S} + \beta|0\rangle_{\omega_A}|1\rangle_{\omega_S}$ ,  $\forall \alpha, \beta$ , has no coherences in the Fock basis. In other words, the radiation emitted into each of the modes consists of a statistical mixture of vacuum and single photons; as such, it has a random phase and an amplitude averaging to zero. To characterize the emitted radiation with amplitude measurements, we thus introduce a variation of the pulse sequence [Fig. 3(b)]. We introduce the vacuum energy level  $|0\rangle_{\omega_A}|0\rangle_{\omega_S}$  to the state by applying two  $\pi/2$  pulses and a  $\pi$  pulse, followed by the two drives to obtain the propagating state  $\frac{1}{2}|0\rangle_{\omega_A}|0\rangle_{\omega_S} + \frac{1}{\sqrt{2}}|1\rangle_{\omega_A}|0\rangle_{\omega_S} + \frac{1}{2}|0\rangle_{\omega_A}|1\rangle_{\omega_S}$ . The emitted photon amplitude of the two frequency modes has a fast rise followed by an exponential decay [Fig. 3(c)], where the speed of the photon emission, or the effective decay rate, is controlled by adjusting the drive strengths  $\eta$  and  $\zeta$  in Eq. (1).

*Characterization of frequency-bin-encoded photons.*— We characterize the photonic modes through temporal mode matching [41] and joint quantum state tomography. Using temporal mode matching, we select the desired propagating modes  $\hat{a}_A$  and  $\hat{a}_S$  from the continuum of modes in the waveguide, following the method described in Ref. [42] (see SM [36] Sec. III for details). The moments of the two photonic modes are measured when Qubit D is initialized in the state  $\alpha|g\rangle_D + \beta|e\rangle_D$  for different values ( $\alpha, \beta$ ) achieved by sweeping the Rabi angle  $\theta$ , where  $\alpha = \cos(\theta/2)$  and  $\beta = \sin(\theta/2)$  [see Fig. 4(a) for the pulse sequence and Fig. 4(b) for the moments]. As mentioned, the first-order moments representing the mean amplitude of the field,  $\langle \hat{a}_A \rangle$  and  $\langle \hat{a}_S \rangle$ , are always zero because the reduced density matrix of each mode has no coherences.

The mean photon numbers of the field are represented by  $\langle \hat{a}_A^\dagger \hat{a}_A \rangle$  and  $\langle \hat{a}_S^\dagger \hat{a}_S \rangle$ , reaching the maximum values

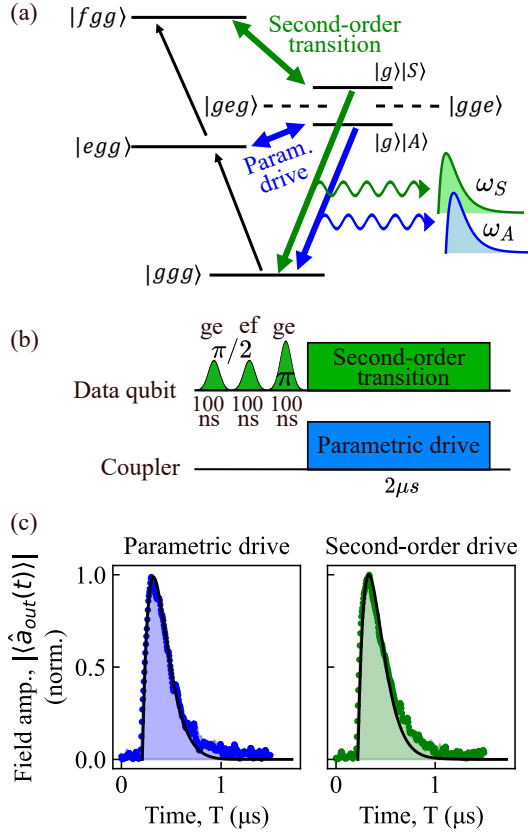


FIG. 3. The emitted frequency-bin-encoded photonic modes. (a) Energy-level diagram illustrating the emission process. The state  $|ijk\rangle$  ( $i, j, k = g, e, f$ ) refers to the states of Qubit D, the coupler, and Qubit E, respectively. (b) Pulse sequence for generating a frequency-bin-encoded photon with a non-zero amplitude. (c) The amplitude of the frequency-bin-encoded photonic modes. The filled circles represent the measured photon magnitude when the photonic modes are emitted simultaneously using the parametric and second-order-transition drives. The shaded area represents the measured photon magnitude when each drive pulse is applied individually and each photon is measured separately. The solid black curves represent the theoretical prediction of the photon magnitude obtained from numerical simulations.

when Qubit D is initialized in  $|g\rangle_D$  and  $|e\rangle_D$ , respectively.  $\langle \hat{a}_S^\dagger \hat{a}_S \rangle$  is expected to be zero when the Rabi angle  $\theta$  is 0; however, it is finite due to the thermal excitation of Qubit D. Similarly,  $\langle \hat{a}_A^\dagger \hat{a}_A \rangle$  should be zero when  $\theta$  is  $\pi$ , but it remains nonzero because of the decoherence of Qubit D. In the first case, all population of Qubit D is transferred into the photon state  $|1\rangle_{\omega_A} |0\rangle_{\omega_S}$ , while in the latter case, all population of Qubit D is transferred into the state  $|0\rangle_{\omega_A} |1\rangle_{\omega_S}$ . The cross-correlated second-order moment of the two modes,  $\langle \hat{a}_A^\dagger \hat{a}_S \rangle$ , signals entanglement between the two photonic modes, which reaches the maximum at  $\theta = \pi/2$  when we get an equal superposition state between the two modes,  $\frac{1}{\sqrt{2}}(|1\rangle_{\omega_A} |0\rangle_{\omega_S} + |0\rangle_{\omega_A} |1\rangle_{\omega_S})$ . The other cross-correlated moment  $\langle \hat{a}_A \hat{a}_S \rangle$  is zero for all Rabi angles, because the two photons are never emitted at the

same time. The fourth-order moments  $\langle (\hat{a}_A^\dagger)^2 \hat{a}_A^2 \rangle$  and  $\langle (\hat{a}_S^\dagger)^2 \hat{a}_S^2 \rangle$  are expected to be zero for all  $\theta$  since maximally a single photon is emitted in each mode. The cross-correlated fourth-order moment  $\langle \hat{a}_A^\dagger \hat{a}_A \hat{a}_S^\dagger \hat{a}_S \rangle$  is also zero, as the information is encoded into the superposition state  $\alpha |1\rangle_{\omega_A} |0\rangle_{\omega_S} + \beta |0\rangle_{\omega_A} |1\rangle_{\omega_S}$  for any Rabi angle  $\theta$ , where the absence of simultaneous photon occupation in both modes ensures that no joint detection is possible.

By initializing Qubit D in states  $|g\rangle_D$ ,  $\frac{1}{\sqrt{2}}(|g\rangle_D + |e\rangle_D)$ , and  $|e\rangle_D$ , bringing them to higher excited state to emit via the hybridized emitter, and performing joint quantum state tomography, we reconstruct the density matrices of the frequency-bin-encoded photonic modes for the three cases [Fig. 4(c-e)]. In the reconstruction, we use least-squares optimization [43, 44] to find the most likely density matrix of the frequency-bin-encoded photonic modes corresponding to the measured moments. The fidelity of the density matrix is defined as  $F(\rho_{ideal}, \rho) = (\text{Tr} \sqrt{\sqrt{\rho_{ideal}} \rho \sqrt{\rho_{ideal}}})^2$  [45], with  $\rho_{ideal}$  being the expected density matrix and  $\rho$  being the measured density matrix. The obtained fidelities of the density matrices are 90.0%, 87.1%, and 83.1%, for the three photonic states  $|1\rangle_{\omega_A} |0\rangle_{\omega_S}$ ,  $\frac{1}{\sqrt{2}}(|1\rangle_{\omega_A} |0\rangle_{\omega_S} + |0\rangle_{\omega_A} |1\rangle_{\omega_S})$ , and  $|0\rangle_{\omega_A} |1\rangle_{\omega_S}$ , respectively. The simulated density matrices of the same three states yield fidelities of 95.5%, 95.2%, and 95.1%, respectively, considering the longitudinal and transverse relaxation of Qubit D and the coupler. Note that the thermal noise is not taken into account in the simulation, which also leads to the infidelity.

The quantum process tomography is done by initializing Qubit D in one more state,  $\frac{1}{\sqrt{2}}(|g\rangle_D - i|e\rangle_D)$ , in addition to the three states above, which correspond to the cardinal states on the Bloch sphere. We then utilize the reconstructed density matrices of the frequency-bin-encoded photons for these four states, along with least-squares optimization, to determine the process matrix  $\chi$  [46]. The process fidelity is found to be 90.4% [Fig. 4(e)] (see SM [36] Sec. III for details on both state and process tomography).

TABLE I. Frequency-bin encoding as an error-detection protocol for photon loss. If any of the two modes get lost before absorbing, the state of Qubit D at the receiver's processor will end up in the second excited state,  $|f\rangle$ .

	Transmitted photon state	Qubit at the receiver
Success	$\alpha  1\rangle_{\omega_A}  0\rangle_{\omega_S} + \beta  0\rangle_{\omega_A}  1\rangle_{\omega_S}$	$\alpha  g\rangle_D + \beta  e\rangle_D$
Error	$ 0\rangle_{\omega_A}  0\rangle_{\omega_S}$	$ f\rangle_D$

*Discussion*— In this work, we experimentally demonstrated the generation of frequency-bin-encoded photonic modes in microwave regime. The two propagating modes, emitted simultaneously at different frequencies, enable error detection against photon loss in distributed quantum computing. By leveraging the hybridized emitter formed by the coupler and Qubit E, and applying both

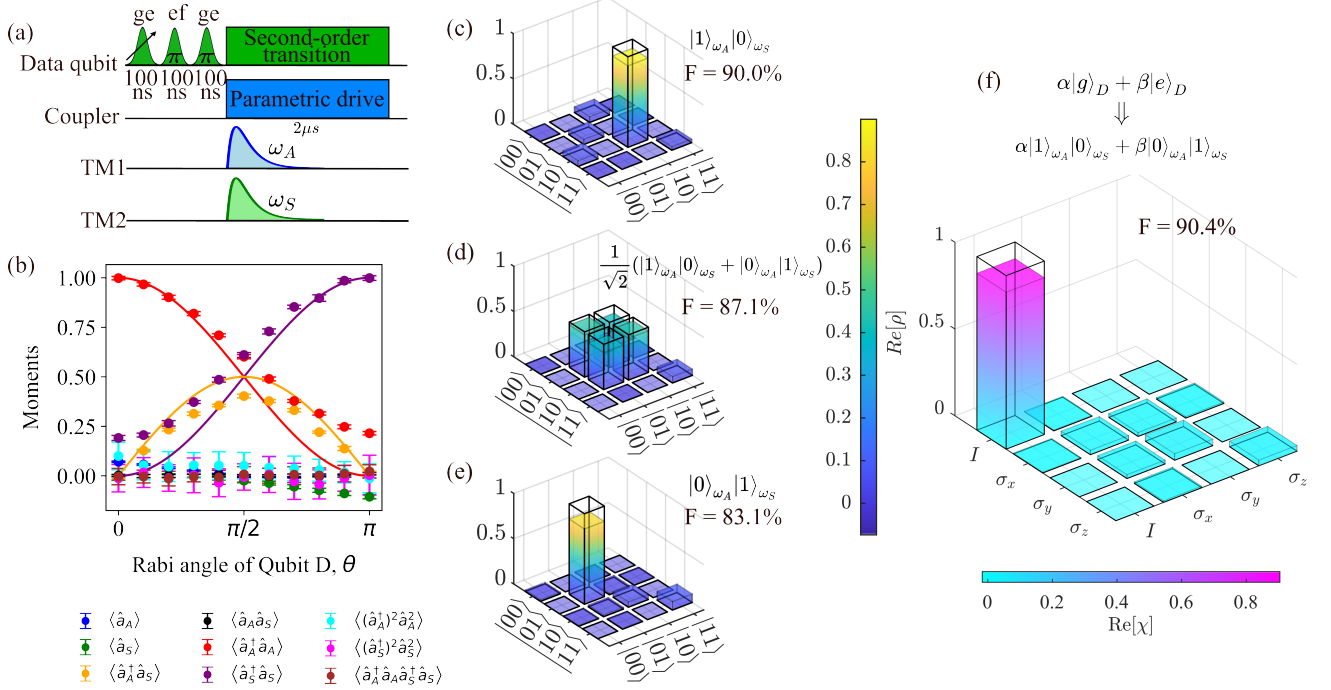


FIG. 4. Tomography measurement of the frequency-bin-encoded photon output field. (a) Pulse sequence for the tomography measurement. TM1 and TM2 are the two temporal filters for temporal mode matching. (b) Selected first- to fourth-order moments of the emitted photon field. The filled circles are the measured data, and the solid curves represent the expected values of the corresponding-colored moments. Those moments without a solid curve in the same colors have their expected values to be zero for any Rabi angle  $\theta$ . (c-e) The reconstructed (colored bars) and expected (black wireframes) density matrices of the frequency-bin-encoded propagating modes for Qubit D initially in the states (c)  $|g\rangle_D$ , (d)  $\frac{1}{\sqrt{2}}(|g\rangle_D + |e\rangle_D)$ , and (e)  $|e\rangle_D$ . The fidelity  $F$  between the reconstructed and expected matrices is indicated next to each corresponding density matrix. The imaginary components of the reconstructed density matrices are not shown; they are less than 0.1 across all elements of the matrices. (f) The process matrix  $\chi$  for state transfer between qubit D and the propagating modes, obtained from quantum process tomography measurements. The colored bars represent the measured results, while the black wireframes depict the ideal process. The imaginary components of the reconstructed  $\chi$  are not shown; they are less than 0.03 across all elements of the matrices.

excitation-preserving and non-preserving drives simultaneously, we achieved two-mode emission from a single qubit physically coupled to a waveguide. This approach eliminates the need for an additional emitter qubit, making the system more hardware-efficient. Additionally, this setup enables photon emission both with and without frequency-bin encoding from the same device, allowing us to encode quantum information into photonic modes while maintaining the flexibility to integrate or bypass the error-detection protocol using the same system. The fidelity of the operation is limited by decoherence to 95%, theoretically; however, our measurements indicate a lower fidelity of 90%. This 5% reduction is primarily attributed to two factors: approximately 2% arises from coherent errors in the control pulses used to drive transitions between the data qubit and the hybridized emitter (see SM [36] Sec. IIID for the reconstruction considering only coherent errors), and the rest is due to thermal excitation of the data qubit at the start of the protocol. Thermal excitation can be mitigated through active or passive qubit reset [47, 48], while coherent errors can

be reduced by employing accurate modeling and optimal control techniques [49, 50]. This frequency-bin-encoded photon generation method is also applicable to other types of solid-state quantum hardware, such as quantum dots [51].

To demonstrate a distributed quantum computing architecture with frequency-bin-encoded photons, we can reshape the envelopes of the photonic modes to be time-symmetric as in Ref. [32, 39], and use the same structure for photon re-absorption, in a time-reversed way. If any mode is lost during the transmission or not successfully absorbed by the receiver, a vacuum state is received instead of the desired state of the frequency-bin-encoded state. Receiving the vacuum state results in Qubit D at the receiver ending up in the  $|f\rangle_D$  state, instead of the desired state  $\alpha|g\rangle_D + \beta|e\rangle_D$  (see Table I and SM [36] Sec. IV for details). A quantum non-demolition measurement [52–54] that distinguishes between the  $|f\rangle$  state and a subspace comprising the  $|g\rangle$  state and the  $|e\rangle$  state, without measuring within that subspace, can detect whether there has been photon loss, without af-

fecting the quantum state of a successfully transmitted frequency-bin-encoded pair. Therefore, in quantum state transfer, we can utilize frequency-bin-encoded photonic modes as an error-detection protocol to identify photon loss and resend the quantum information. Remote entanglement can be achieved by employing an extra qubit in the quantum processor connected to the emitter node of the distributed quantum computing system (see SM [36] Sec. IV for details). Similarly, any photon loss during the transfer will result in Qubit D at the receiver ending up in  $|f\rangle_D$ . Our work is thus a building block for distributed quantum computing architecture and quantum networks.

*Author contributions.*— S.G. planned the project. J.Y. performed the experiments and analyzed the data with input from A.M.E., I.S., S.G., and M.A.U.. M.K. and G.J. built the theoretical model. J.Y. designed the device and C.C.M. fabricated the device. A.G. and A.F.K. operated the quantum state tomography and quantum process tomography. J.Y. and M.K. wrote the manuscript

with feedback from all authors. S.G. and A.M.E. supervised this work.

*Acknowledgments.*— The authors thank Mohammed Ali Aamir for useful discussions, and Lars Jönsson for his help in making the sample holders. The device in this work was fabricated in Myfab, Chalmers, a micro- and nano-fabrication laboratory. The traveling-wave parametric amplifier (TWPA) used in this experiment was provided by IARPA and Lincoln Labs. This work was supported by Ericsson Research and the Knut and Alice Wallenberg Foundation through the Wallenberg Centre for Quantum Technology (WACQT). S.G. acknowledges financial support from the European Research Council via Grant No. 101041744 ESQuAT. A.F.K. is also supported by the Swedish Research Council (grant number 2019-03696), the Swedish Foundation for Strategic Research (grant numbers FFL21-0279 and FUS21-0063), and the Horizon Europe program HORIZON-CL4-2022-QUANTUM-01-SGA via the project 101113946 OpenSuperQPlus100.

- 
- [1] J. I. Cirac, P. Zoller, H. J. Kimble, and H. Mabuchi, Quantum state transfer and entanglement distribution among distant nodes in a quantum network, *Physical Review Letters* **78**, 3221 (1997).
- [2] H. J. Kimble, The quantum internet, *Nature* **453**, 1023 (2008).
- [3] V. Krutyanskiy, M. Galli, V. Krcmarsky, S. Baier, D. A. Fioretto, Y. Pu, A. Mazloom, P. Sekatski, M. Canteri, M. Teller, J. Schupp, J. Bate, M. Meraner, N. Sangouard, B. P. Lanyon, and T. E. Northup, Entanglement of trapped-ion qubits separated by 230 meters, *Physical Review Letters* **130**, 050803 (2023).
- [4] J. Hofmann, M. Krug, N. Ortegel, L. Gérard, M. Weber, W. Rosenfeld, and H. Weinfurter, Heralded entanglement between widely separated atoms, *Science* **337**, 72 (2012).
- [5] S. Ritter, C. Nölleke, C. Hahn, A. Reiserer, A. Neuzner, M. Uphoff, M. Mücke, E. Figueroa, J. Bochmann, and G. Rempe, An elementary quantum network of single atoms in optical cavities, *Nature* **484**, 195 (2012).
- [6] A. Delteil, Z. Sun, W.-b. Gao, E. Togan, S. Faelt, and A. Imamoglu, Generation of heralded entanglement between distant hole spins, *Nature Physics* **12**, 218 (2016).
- [7] R. Stockill, M. J. Stanley, L. Huthmacher, E. Clarke, M. Hugues, A. J. Miller, C. Matthiesen, C. Le Gall, and M. Atatüre, Phase-tuned entangled state generation between distant spin qubits, *Physical Review Letters* **119**, 010503 (2017).
- [8] H. Bernien, B. Hensen, W. Pfaff, G. Koolstra, M. S. Blok, L. Robledo, T. H. Taminiau, M. Markham, D. J. Twitchen, L. Childress, *et al.*, Heralded entanglement between solid-state qubits separated by three metres, *Nature* **497**, 86 (2013).
- [9] P. C. Humphreys, N. Kalb, J. P. Morits, R. N. Schouten, R. F. Vermeulen, D. J. Twitchen, M. Markham, and R. Hanson, Deterministic delivery of remote entanglement on a quantum network, *Nature* **558**, 268 (2018).
- [10] N. Leung, Y. Lu, S. Chakram, R. Naik, N. Earnest, R. Ma, K. Jacobs, A. Cleland, and D. Schuster, Deterministic bidirectional communication and remote entanglement generation between superconducting qubits, *npj Quantum Information* **5**, 18 (2019).
- [11] Y. Zhong, H.-S. Chang, A. Bienfait, É. Dumur, M.-H. Chou, C. R. Conner, J. Grebel, R. G. Povey, H. Yan, D. I. Schuster, *et al.*, Deterministic multi-qubit entanglement in a quantum network, *Nature* **590**, 571 (2021).
- [12] P. Campagne-Ibarcq, E. Zalys-Geller, A. Narla, S. Shankar, P. Reinhold, L. Burkhardt, C. Axline, W. Pfaff, L. Frunzio, R. J. Schoelkopf, and M. H. Devoret, Deterministic remote entanglement of superconducting circuits through microwave two-photon transitions, *Physical Review Letters* **120**, 200501 (2018).
- [13] P. Kurpiers, P. Magnard, T. Walter, B. Royer, M. Pechal, J. Heinsoo, Y. Salathé, A. Akin, S. Storz, J.-C. Besse, *et al.*, Deterministic quantum state transfer and remote entanglement using microwave photons, *Nature* **558**, 264 (2018).
- [14] C. J. Axline, L. D. Burkhardt, W. Pfaff, M. Zhang, K. Chou, P. Campagne-Ibarcq, P. Reinhold, L. Frunzio, S. Girvin, L. Jiang, *et al.*, On-demand quantum state transfer and entanglement between remote microwave cavity memories, *Nature Physics* **14**, 705 (2018).
- [15] P. Magnard, S. Storz, P. Kurpiers, J. Schär, F. Marxer, J. Lütolf, T. Walter, J.-C. Besse, M. Gabureac, K. Reuer, A. Akin, B. Royer, A. Blais, and A. Wallraff, Microwave quantum link between superconducting circuits housed in spatially separated cryogenic systems, *Physical Review Letters* **125**, 260502 (2020).
- [16] J. Qiu, Y. Liu, J. Niu, L. Hu, Y. Wu, L. Zhang, W. Huang, Y. Chen, J. Li, S. Liu, *et al.*, Deterministic quantum teleportation between distant superconducting chips, *arXiv preprint arXiv:2302.08756* (2023).
- [17] J. Grebel, H. Yan, M.-H. Chou, G. Andersson, C. R. Conner, Y. J. Joshi, J. M. Miller, R. G. Povey, H. Qiao, X. Wu, and A. N. Cleland, Bidirectional multiphoton communication between remote superconducting nodes, *Physical Review Letters* **132**, 047001 (2024).

- [18] H.-P. Lo, T. Ikuta, N. Matsuda, T. Honjo, W. J. Munro, and H. Takesue, Quantum process tomography of a controlled-phase gate for time-bin qubits, *Physical Review Applied* **13**, 034013 (2020).
- [19] S. Saha, M. Shalae, J. O'Reilly, I. Goetting, G. Toh, A. Kalakuntla, Y. Yu, and C. Monroe, High-fidelity remote entanglement of trapped atoms mediated by time-bin photons, *arXiv preprint arXiv:2406.01761* (2024).
- [20] J. M. Lukens and P. Lougovski, Frequency-encoded photonic qubits for scalable quantum information processing, *Optica* **4**, 8 (2017).
- [21] H.-H. Lu, E. M. Simmerman, P. Lougovski, A. M. Weiner, and J. M. Lukens, Fully arbitrary control of frequency-bin qubits, *Physical Review Letters* **125**, 120503 (2020).
- [22] H.-H. Lu, M. Liscidini, A. L. Gaeta, A. M. Weiner, and J. M. Lukens, Frequency-bin photonic quantum information, *Optica* **10**, 1655 (2023).
- [23] N. A. Peters, J. T. Barreiro, M. E. Goggin, T.-C. Wei, and P. G. Kwiat, Remote state preparation: Arbitrary remote control of photon polarization, *Physical Review Letters* **94**, 150502 (2005).
- [24] P. Kok, H. Lee, and J. P. Dowling, Creation of large-photon-number path entanglement conditioned on photodetection, *Physical Review A* **65**, 052104 (2002).
- [25] J. C. F. Matthews, A. Politi, D. Bonneau, and J. L. O'Brien, Heralding two-photon and four-photon path entanglement on a chip, *Physical Review Letters* **107**, 163602 (2011).
- [26] A. M. Yao and M. J. Padgett, Orbital angular momentum: origins, behavior and applications, *Advances in Optics and Photonics* **3**, 161 (2011).
- [27] J. Ilves, S. Kono, Y. Sunada, S. Yamazaki, M. Kim, K. Koshino, and Y. Nakamura, On-demand generation and characterization of a microwave time-bin qubit, *npj Quantum Information* **6**, 34 (2020).
- [28] P. Kurpiers, M. Pechal, B. Royer, P. Magnard, T. Walter, J. Heinsoo, Y. Salathé, A. Akin, S. Storz, J.-C. Besse, S. Gasparinetti, A. Blais, and A. Wallraff, Quantum communication with time-bin encoded microwave photons, *Physical Review Applied* **12**, 044067 (2019).
- [29] Y. Li, Z. Wang, Z. Bao, Y. Wu, J. Wang, J. Yang, H. Xiong, Y. Song, H. Zhang, and L. Duan, Frequency-tunable microwave quantum light source based on superconducting quantum circuits, *Chip* **2**, 100063 (2023).
- [30] J.-C. Besse, K. Reuer, M. C. Collodo, A. Wulff, L. Wernli, A. Copetudo, D. Malz, P. Magnard, A. Akin, M. Gabureac, *et al.*, Realizing a deterministic source of multipartite-entangled photonic qubits, *Nature communications* **11**, 4877 (2020).
- [31] B. Kannan, A. Almanakly, Y. Sung, A. Di Paolo, D. A. Rower, J. Braumüller, A. Melville, B. M. Niedzielski, A. Karamlou, K. Serniak, *et al.*, On-demand directional microwave photon emission using waveguide quantum electrodynamics, *Nature Physics* **19**, 394 (2023).
- [32] J. Yang, A. M. Eriksson, M. A. Aamir, I. Strandberg, C. Castillo-Moreno, D. P. Lozano, P. Persson, and S. Gasparinetti, Deterministic generation of shaped single microwave photons using a parametrically driven coupler, *Physical Review Applied* **20**, 054018 (2023).
- [33] R. Barends, J. Kelly, A. Megrant, D. Sank, E. Jeffrey, Y. Chen, Y. Yin, B. Chiaro, J. Mutus, C. Neill, *et al.*, Coherent Josephson qubit suitable for scalable quantum integrated circuits, *Physical Review Letters* **111**, 080502 (2013).
- [34] J. Koch, T. M. Yu, J. Gambetta, A. A. Houck, D. I. Schuster, J. Majer, A. Blais, M. H. Devoret, S. M. Girvin, and R. J. Schoelkopf, Charge-insensitive qubit design derived from the Cooper pair box, *Physical Review A* **76**, 042319 (2007).
- [35] D. C. McKay, S. Filipp, A. Mezzacapo, E. Magesan, J. M. Chow, and J. M. Gambetta, Universal gate for fixed-frequency qubits via a tunable bus, *Physical Review Applied* **6**, 064007 (2016).
- [36] See supplemental material.
- [37] S. Filipp, A. F. van Loo, M. Baur, L. Steffen, and A. Wallraff, Preparation of subradiant states using local qubit control in circuit qed, *Physical Review A* **84**, 061805 (2011).
- [38] M. A. Aamir, C. C. Moreno, S. Sundelin, J. Biznárová, M. Scigliuzzo, K. E. Patel, A. Osman, D. P. Lozano, I. Strandberg, and S. Gasparinetti, Engineering symmetry-selective couplings of a superconducting artificial molecule to microwave waveguides, *Physical Review Letters* **129**, 123604 (2022).
- [39] M. Pechal, L. Huthmacher, C. Eichler, S. Zeytinoglu, A. A. Abdumalikov, S. Berger, A. Wallraff, and S. Filipp, Microwave-controlled generation of shaped single photons in Circuit Quantum Electrodynamics, *Physical Review X* **4**, 041010 (2014).
- [40] M. Roth, M. Ganzhorn, N. Moll, S. Filipp, G. Salis, and S. Schmidt, Analysis of a parametrically driven exchange-type gate and a two-photon excitation gate between superconducting qubits, *Physical Review A* **96**, 062323 (2017).
- [41] C. Eichler, D. Bozyigit, C. Lang, L. Steffen, J. Fink, and A. Wallraff, Experimental state tomography of itinerant single microwave photons, *Physical Review Letter* **106**, 220503 (2011).
- [42] C. Eichler, D. Bozyigit, and A. Wallraff, Characterizing quantum microwave radiation and its entanglement with superconducting qubits using linear detectors, *Physical Review A* **86**, 032106 (2012).
- [43] R. Nehra, M. Eaton, C. González-Arciniegas, M. S. Kim, T. Gerrits, A. Lita, S. W. Nam, and O. Pfister, Generalized overlap quantum state tomography, *Physical Review Research* **2**, 042002 (2020).
- [44] I. Strandberg, Simple, reliable, and noise-resilient continuous-variable quantum state tomography with convex optimization, *Physical Review Applied* **18**, 044041 (2022).
- [45] R. Jozsa, Fidelity for mixed quantum states, *Journal of Modern Optics* **41**, 2315 (1994).
- [46] A. Gaikwad, K. Shende, Arvind, and K. Dorai, Implementing efficient selective quantum process tomography of superconducting quantum gates on IBM quantum experience, *Scientific Reports* **12**, 3688 (2022).
- [47] P. Magnard, P. Kurpiers, B. Royer, T. Walter, J.-C. Besse, S. Gasparinetti, M. Pechal, J. Heinsoo, S. Storz, A. Blais, *et al.*, Fast and unconditional all-microwave reset of a superconducting qubit, *Physical review letters* **121**, 060502 (2018).
- [48] M. A. Aamir, P. J. Suria, J. A. M. Guzmán, C. Castillo-Moreno, J. M. Epstein, N. Y. Halpern, and S. Gasparinetti, Thermally driven quantum refrigerator autonomously resets superconducting qubit, *arXiv preprint arXiv:2305.16710* <https://doi.org/10.48550/arXiv.2305.16710> (2023).

- [49] F. Motzoi, J. M. Gambetta, P. Rebentrost, and F. K. Wilhelm, Simple pulses for elimination of leakage in weakly nonlinear qubits, [Physical review letters](#) **103**, 110501 (2009).
- [50] M. Werninghaus, D. J. Egger, F. Roy, S. Machnes, F. K. Wilhelm, and S. Filipp, Leakage reduction in fast superconducting qubit gates via optimal control, [npj Quantum Information](#) **7**, 14 (2021).
- [51] A. Stockklauser, P. Scarlino, J. V. Koski, S. Gasparinetti, C. K. Andersen, C. Reichl, W. Wegscheider, T. Ihn, K. Ensslin, and A. Wallraff, Strong coupling cavity QED with gate-defined double quantum dots enabled by a high impedance resonator, [Physical Review X](#) **7**, 011030 (2017).
- [52] N. Ofek, A. Petrenko, R. Heeres, P. Reinhold, Z. Leghtas, B. Vlastakis, Y. Liu, L. Frunzio, S. M. Girvin, L. Jiang, *et al.*, Extending the lifetime of a quantum bit with error correction in superconducting circuits, [Nature](#) **536**, 441 (2016).
- [53] S. Kono, K. Koshino, Y. Tabuchi, A. Noguchi, and Y. Nakamura, Quantum non-demolition detection of an itinerant microwave photon, [Nature Physics](#) **14**, 546 (2018).
- [54] J.-C. Besse, S. Gasparinetti, M. C. Collodo, T. Walter, P. Kurpiers, M. Pechal, C. Eichler, and A. Wallraff, Single-shot quantum nondemolition detection of individual itinerant microwave photons, [Physical Review X](#) **8**, 021003 (2018).



# Deterministic generation of frequency-bin-encoded microwave photons — Supplementary Material

Jiaying Yang<sup>1,2</sup>, Maryam Khanahmadi<sup>1</sup>, Ingrid Strandberg<sup>1</sup>, Akshay Gaikwad<sup>1</sup>, Claudia Castillo-Moreno<sup>1</sup>, Anton Frisk Kockum<sup>1</sup>, Muhammad Asad Ullah<sup>2</sup>, Göran Johansson<sup>1</sup>, Axel Martin Eriksson<sup>1</sup>, Simone Gasparinetti<sup>1</sup>

<sup>1</sup>*Department of Microtechnology and Nanoscience,  
Chalmers University of Technology, SE-412 96, Göteborg, Sweden*  
<sup>2</sup>*Ericsson Research, Ericsson AB, SE-164 83, Stockholm, Sweden*

## I. MEASUREMENT DETAILS

In this work, we utilize a  $6.6 \times 6.6 \text{ mm}^2$  superconducting device. The device is fabricated on a silicon substrate, and its RF lines and ground plane consist of aluminium layers deposited on top of the substrate. We wire-bond the device in a copper sample holder, which is then enclosed within a copper shield. To provide additional protection against magnetic interference, we place the bonded device inside another  $\mu$ -metal shield (cryoperm). This shielding is installed in the mixing chamber of a dilution refrigerator to ensure that all experimental measurements are conducted at temperatures below 15 mK (Fig. S1).

The device is controlled with one transmission line, one charge line, two flux lines, and one reflection input and output line at the waveguide. The two  $\lambda/4$  resonators are coupled to the transmission line to read out the state of qubit D and the coupler. The charge line, capacitively coupled to qubit D, is used both for preparing the desired quantum state for transfer and for applying the second-order-transition drive. The flux lines, which are inductively coupled to the coupler and the SQUID loops of qubit E, enable frequency tunability. Additionally, we use the flux line connected to the coupler to apply the parametric drive. The waveguide capacitively coupled to Qubit E connects to the reflection input and output lines on the other side, from where the emitted photon field is measured via a traveling-wave parametric amplifier (TWPA) [1], a high-electron-mobility transistor (HEMT) amplifier, and room-temperature amplifiers in the output line. In our system, we measure the quantum efficiency  $\eta$  to be 0.192, where  $\eta = \frac{1/2}{1/2+n_{\text{added}}}$  and  $n_{\text{added}} = 2.1$  is the added noise photon number by the amplification chain.

In the experiment, data are obtained using a pulsed setup. Microwave control pulses are sent to drive the emitter using arbitrary waveform generators (AWGs), and the data are read out with analogue-to-digital converters (ADCs) from the microwave transceiver platform Vivace [2], after up- and down-conversion by IQ mixers and local oscillators. The phase synchronization of the multiple local oscillators and the microwave transceiver is done by connecting them to the same external clock.

The measured parameters of the device are shown in Table I, and the coherence times of qubit D are shown in Table II.  $T_1$  and  $T_2$  are the longitudinal and transverse relaxation times of qubit D, measured when the frequencies of the coupler and Qubit E are at the sweet spot;  $T'_1$  and  $T'_2$  are measured when both components are at the operating point. We measure the coherence times for Qubit D for both the *ge* and *ef* transitions. The relaxation rates of the coupler are measured to be  $T_1 = 2.3 \pm 0.5 \mu\text{s}$  and  $T_2 = 1.4 \pm 0.4 \mu\text{s}$ .

TABLE I. Experimentally measured parameter values.

Parameter	Symbol	Data qubit	Coupler	Emitter qubit
Readout resonator frequency	$f_R/2\pi$ (GHz)	6.19	6.74	–
Decay rate of the resonator to the feedline	$\kappa/2\pi$ (kHz)	523	752	–
Coupling rate between qubit D (coupler) and their readout resonator	$j/2\pi$ (MHz)	69.33	42.34	–
Qubit (coupler) frequency without DC flux bias	$\omega/2\pi$ (GHz)	5.05	8.46	6.17
Qubit (coupler) frequency with DC flux bias to operating point	$\omega'/2\pi$ (GHz)	5.05	5.79	5.70
Anharmonicity of qubit (coupler)	$\alpha/2\pi$ (MHz)	-215	-60	-215
Coupling rate between qubit and coupler	$g/2\pi$ (MHz)	37.5	–	46
Coupling rate between qubit E and the coplanar waveguide	$\Gamma_E/2\pi$ (MHz)	–	–	8.0

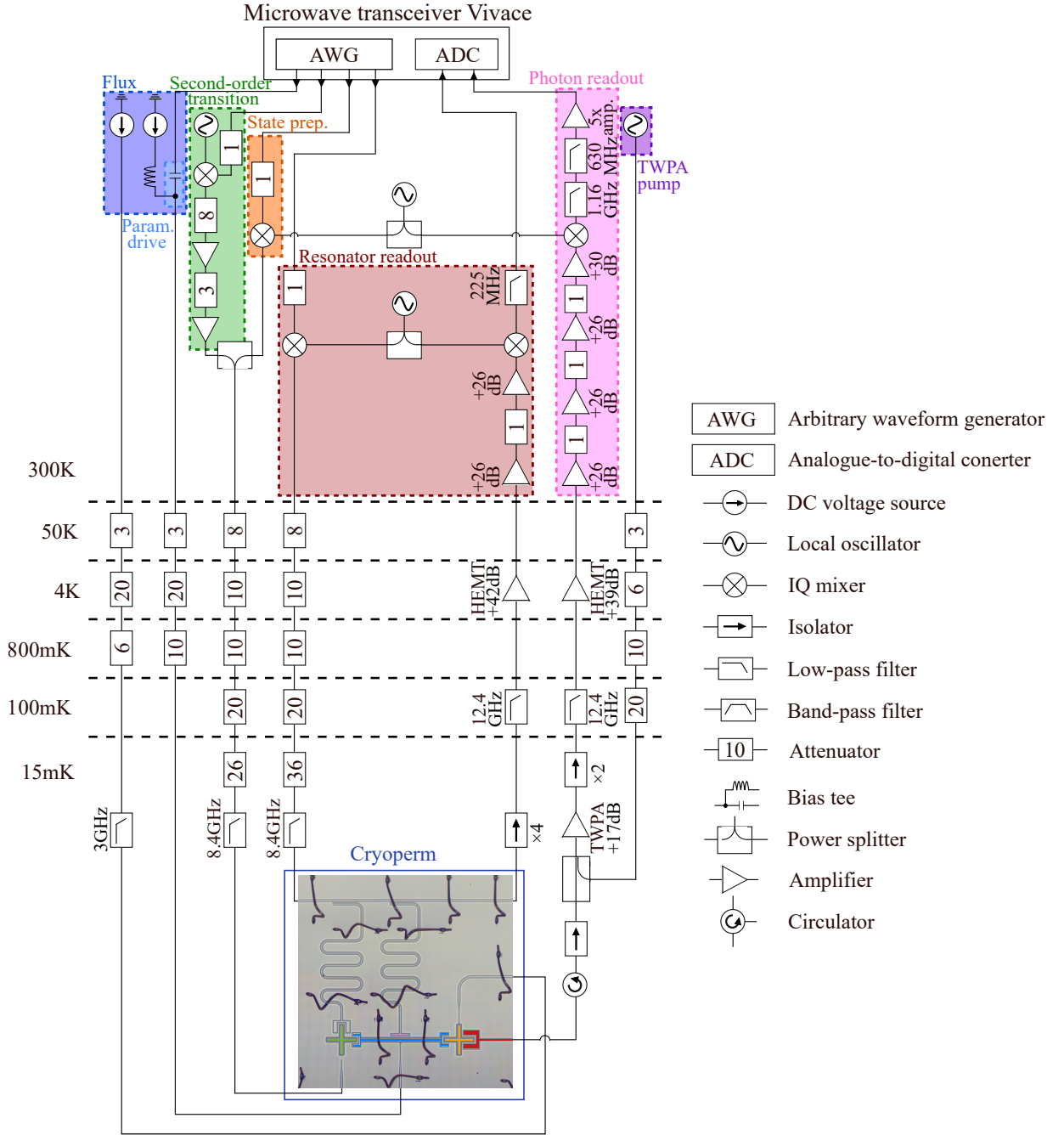


FIG. S1. The wiring diagram illustrating the connection of the superconducting chip to the input and output lines of the experimental setup. Note that both the AWG and ADC have two ports for in-phase (I) and quadrature (Q) components; however, only one port is shown for simplicity. The Vivace microwave transceiver board [2] provides the AWG and ADC channels. Additionally, wire-bonded airbridges (black) are used to ensure a continuous and consistent ground connection, as shown in the device photo.

## II. THEORETICAL MODEL

### A. Bare Hamiltonian

According to Fig. 1 in the main text, we consider Qubit D as a three-level system with frequency  $\omega_D$  and the anharmonicity  $\alpha = 2\chi_d$  and the coupler and Qubit E as two-level systems, since large anharmonicity suppresses populating the higher energy levels. In the following, we consider the annihilation and creation operators  $\{(\hat{d}, \hat{d}^\dagger), (\hat{e}, \hat{e}^\dagger), (\hat{c}, \hat{c}^\dagger)\}$ ,

TABLE II. The coherence times of Qubit D. We have larger  $T_{1,ef}$  than  $T_{1,ge}$ , which can be attributed to the weaker coupling of the system to the environment at  $\omega_D^{ef}$  compared to  $\omega_D^{ge}$ .

$T_1$ ( $\mu\text{s}$ )				$T_2$ ( $\mu\text{s}$ )			
Sweet spot		Operating spot		Sweet spot		Operating spot	
$T_{1,ge}$	$T_{1,ef}$	$T'_{1,ge}$	$T'_{1,ef}$	$T_{2,ge}$	$T_{2,ef}$	$T'_{2,ge}$	$T'_{2,ef}$
$21.7 \pm 3.6$	$27.0 \pm 3.0$	$20.8 \pm 2.5$	$27.0 \pm 3.0$	$5.7 \pm 0.7$	$4.4 \pm 0.5$	$14.0 \pm 3.4$	$8.8 \pm 1.4$

which correspond to Qubit D, the coupler, and Qubit E, respectively. Considering the same frequency for the emitter and the coupler as  $\omega_E$  and assuming the coupling between the coupler and Qubit D (E) as  $g_{dc}$  ( $g_{ec}$ ), the total Hamiltonian in the lab frame is obtained as

$$H = \omega_D \hat{d}^\dagger \hat{d} + \omega_E \hat{e}^\dagger \hat{e} + (\omega_E + \omega_{\text{ext}}(t)) \hat{c}^\dagger \hat{c} + \chi_d \hat{d}^{\dagger 2} \hat{d}^2 + g_{dc} (\hat{d} + \hat{d}^\dagger) (\hat{c} + \hat{c}^\dagger) + g_{ec} (\hat{e} + \hat{e}^\dagger) (\hat{c} + \hat{c}^\dagger) + \zeta' (e^{i(2\omega_d + 2\chi_d - (\omega_e + \delta))} \hat{d} + e^{-i(2\omega_d + 2\chi_d - (\omega_e + \delta))} \hat{d}^\dagger), \quad (\text{S1})$$

where  $\omega_{\text{ext}}(t)$  is the time-dependent frequency corresponding to the flux drive of the coupler and the amplitude of drive on Qubit D is considered to be  $\zeta'$ . Note that  $g_{ec}$  is written as  $g$  in the main text for simplicity. Introducing two hybridized modes, symmetric  $\hat{a}_S = (\hat{e} + \hat{c})/\sqrt{2}$  and antisymmetric  $\hat{a}_A = (\hat{e} - \hat{c})/\sqrt{2}$ , respectively, the Hamiltonian changes to

$$H = \omega_D \hat{d}^\dagger \hat{d} + \omega_S \hat{a}_S^\dagger \hat{a}_S + \omega_A \hat{a}_A^\dagger \hat{a}_A + \frac{g_{dc}}{\sqrt{2}} [\hat{d}^\dagger (\hat{a}_S - \hat{a}_A) + (\hat{a}_S - \hat{a}_A)^\dagger \hat{d}] + \frac{\omega_{\text{ext}}(t)}{2} (\hat{a}_S - \hat{a}_A)^\dagger (\hat{a}_S - \hat{a}_A) + \chi_d \hat{d}^{\dagger 2} \hat{d}^2 + \zeta' (e^{i(2\omega_d + 2\chi_d - \omega_S)} \hat{d} + e^{-i(2\omega_d + 2\chi_d - \omega_S)} \hat{d}^\dagger), \quad (\text{S2})$$

where the hybridized frequencies are  $\omega_S = (\omega_E + g_{ec})$  and  $\omega_A = (\omega_E - g_{ec})$ . The frequency of the coupler is evaluated as

$$\omega_C(t) = \omega_c^0 \sqrt{\left| \cos\left(\frac{\pi\phi(t)}{\phi_0}\right) \right|} \equiv \omega_E + \omega_{\text{ext}}(t) \rightarrow \pi\phi(t)/\phi_0 = \varphi_{dc} + \eta' \cos(\omega_d t), \quad (\text{S3})$$

where in a weak modulation drive, the Taylor expansion of the coupler frequency leads to

$$\omega_E(t) = \omega_c^0 \sqrt{|\cos(\varphi_{dc})|}, \quad (\text{S4})$$

$$\omega_{\text{ext}}(t) = \frac{\partial \omega_C}{\partial \varphi} \Big|_{\varphi=\varphi_{dc}} \eta' \cos((\omega_E - \omega_D)t) + \frac{1}{2} \frac{\partial^2 \omega_C}{\partial \varphi^2} \Big|_{\varphi=\varphi_{dc}} \eta'^2 \cos^2((\omega_E - \omega_D)t). \quad (\text{S5})$$

The emitter qubit is strongly coupled to a waveguide with strength  $L = \sqrt{\Gamma_E} \hat{e}$ , which in the symmetric and antisymmetric basis changes to  $L = \sqrt{\Gamma_E} \frac{\hat{a}_S + \hat{a}_A}{\sqrt{2}}$ . Applying the secular approximation in the rotating frame of  $\omega_S$  and  $\omega_A$ , leads to two separate decay channels  $L_1 = \sqrt{\frac{\Gamma_E}{2}} \hat{a}_S$ ,  $L_2 = \sqrt{\frac{\Gamma_E}{2}} \hat{a}_A$  with half the decay rate of the original emitter coupling.

## B. Effective Hamiltonian

Utilizing the black-box quantization methods [3], one can find the dressed-mode coefficients from the linear and time-independent parts of the Hamiltonian; the first line of Eq. (S2). Introducing the dressed modes  $\hat{d} = \varphi_d \hat{d} + \varphi_A \hat{a}_A + \varphi_S \hat{a}_S$ ,  $\hat{a}_S = \varphi'_d \hat{d} + \varphi'_A \hat{a}_A + \varphi'_S \hat{a}_S$ , and  $\hat{a}_A = \varphi''_d \hat{d} + \varphi''_A \hat{a}_A + \varphi''_S \hat{a}_S$ , diagonalizing the first line of Eq. (S2), the second line can be written in the basis  $\hat{d}, \hat{a}_A, \hat{a}_S$ . Applying the optimal displacement transformation  $\alpha = \frac{-\zeta}{\omega_d + 2\chi_d - \omega_S} \equiv \epsilon$  on the  $d$  mode, in the rotating frame of  $\omega_D \hat{d}^\dagger \hat{d} + \omega_S \hat{a}_S^\dagger \hat{a}_S + \omega_A \hat{a}_A^\dagger \hat{a}_A$ , the effective Hamiltonian is obtained as

$$H_{\text{eff}} = \eta (\hat{d} \hat{a}_A^\dagger + \hat{a}_A \hat{d}^\dagger) + 2\epsilon \chi_d \varphi_d^3 \varphi_S [e^{-i2\chi_d t} \hat{d}^{\dagger 2} \hat{a}_S + e^{i2\chi_d t} \hat{a}_S^\dagger \hat{d}^2] + \chi_d \varphi_d^4 \hat{d}^{\dagger 2} \hat{d}^2 + 4\chi_d \varphi_d^2 \varphi_S^2 \hat{d}^\dagger \hat{a}_S^\dagger \hat{a}_S + 4\chi_d \varphi_d^2 \varphi_A^2 \hat{d}^\dagger \hat{a}_A^\dagger \hat{a}_A + 4\epsilon^2 \chi_d \varphi_d^4 \hat{d}^\dagger \hat{d} + 4\epsilon^2 \chi_d \varphi_d^2 \varphi_S^2 \hat{a}_S^\dagger \hat{a}_S + 4\epsilon^2 \chi_d \varphi_d^2 \varphi_A^2 \hat{a}_A^\dagger \hat{a}_A + S(\eta(t)) \left[ (\varphi'_d - \varphi''_d)^2 \hat{d}^\dagger \hat{d} + (\varphi'_S - \varphi''_S)^2 \hat{a}_S^\dagger \hat{a}_S + (\varphi'_A - \varphi''_A)^2 \hat{a}_A^\dagger \hat{a}_A \right], \quad (\text{S6})$$

where the amplitude of the parametric and the second-order-transition drive mentioned in the main text Eq. (1) corresponds to

$$\eta = \frac{1}{2} \frac{\partial \omega_c}{\partial \phi} \Big|_{\phi=\phi_{dc}} \eta' (\varphi'_d - \varphi''_d) (\varphi'_A - \varphi''_A), \quad \zeta = 2\epsilon \chi_d \varphi_d^3 \varphi_s e^{-i2\chi_d t}, \quad (\text{S7})$$

respectively, and the Stark shift induced by the parametric drive is obtained as

$$S(\eta') = \frac{1}{4} \frac{\partial^2 \omega_c}{\partial \varphi^2} \Big|_{\varphi=\varphi_{dc}} \eta'^2. \quad (\text{S8})$$

It is important to note that the Stark shift obtained from the second-order-transition drive on Qubit D is comparable to the detuning  $\omega_d - \omega_S$ . To avoid slowing down the release process, we consider the Stark shift in the frequency of both the second-order-transition and parametric drives. Introducing the AC Stark shift on Qubit D,  $\omega_{AC} = 4\epsilon^2 \chi_d \varphi_d^4$ , the frequencies of the parametric and second-order-transition drives change to  $\omega_{\text{param}} = \omega_d - \omega_A + \omega_{AC}$  and  $\omega_{2\text{nd}} = 2\omega_d + 2\chi_d - \omega_S + 2\omega_{AC}$ , respectively, where the amplitudes in Eq. (S7) change to  $\eta \rightarrow \eta e^{-i\omega_{AC}t}$ ,  $\zeta \rightarrow \zeta e^{-i2\omega_{AC}t}$ .

It is worth noting that the second-order-transition and the parametric drives, by applying the mode decomposition method mentioned in [4], are optimized to populate one single mode (wave packet), in each decay channel. To find the mode decomposition of the output fields, we calculate the two-time-correlation function for each channel, symmetric and antisymmetric, with indices S and A, respectively:

$$G_{S(A)}^{(2)}(t_1, t_2) = \langle L_{S(A)}^\dagger(t_1) L_{S(A)}(t_2) \rangle \equiv n_{S(A)} f_{S(A)}(t_1) f_{S(A)}^*(t_2), \quad (\text{S9})$$

where the number of photons per mode is  $n_{S(A)}$  with the corresponding shape  $f_{S(A)}(t)$  utilized in Sec. III A. To simulate the full tomography on the output field, we consider two catching cavities described by the annihilation operators  $\hat{v}_S, \hat{v}_A$  to catch each traveling wave packet  $f_S(t), f_A(t)$ , respectively [5]. This can be achieved by considering the cascaded formalism [6] between the sender, including Qubit D, the symmetric, and the antisymmetric modes, and the two catching cavities by introducing the total Lindblad operator  $L_{S(A)} = \sqrt{\frac{\gamma}{2}} \hat{a}_{S(A)} + g_{S(A)}^*(t) \hat{v}_{S(A)}$ , where the time-dependent decay rate obtained as  $g_{S(A)}(t) = \frac{-f_{S(A)}^*(t)}{\sqrt{\int_0^t dt' |f_{S(A)}|^2}}$ . Considering the cascaded Hamiltonian  $H_{\text{total}} = H_{\text{eff}} + \frac{i\sqrt{\gamma}}{2\sqrt{2}} [g_S^*(t) \hat{a}_S^\dagger \hat{v}_S - g_S(t) \hat{a}_S \hat{v}_S^\dagger] + \frac{i\sqrt{\gamma}}{2\sqrt{2}} [g_A^*(t) \hat{a}_A^\dagger \hat{v}_A - g_A(t) \hat{a}_A \hat{v}_A^\dagger]$  and the total Lindblad operators  $L_S, L_A$ , the final state of the corresponding Lindblad master equation provides the density matrix of the two-mode traveling quantum state, where the sender transitions to the vacuum state and decouples from the traveling wavepacket.

### III. CHARACTERIZATION OF THE FREQUENCY-ENCODED PHOTONIC MODES

#### A. Temporal mode matching

We apply two temporal filters  $f_k(t)$  ( $k = A, S$ ) to the output field, extracting the frequency-bin encoded propagating modes  $\hat{a}_k$  out of the time-dependent output field  $\hat{a}^{\text{out}}(t)$  as [7]

$$\hat{a}_k = \int_{-\infty}^{\infty} dt f_k(t) \hat{a}_{\text{out}}(t), \quad (\text{S10})$$

where  $\hat{a}_{\text{out}}(t)$  is given by the input-output relation [7, 8],  $\hat{a}_{\text{out}}(t) = \sqrt{\Gamma} \hat{\sigma}(t) - \hat{a}_{\text{in}}(t)$ , with  $\hat{a}_{\text{in}}(t)$  the input field.  $f_k(t)$  ( $k = A, S$ ) are the two temporal filters with carrier frequencies  $\omega_A$  and  $\omega_S$  that fulfil

$$f_k(t) = v_k(t) \cdot e^{i(\omega_k t + \phi)}. \quad (\text{S11})$$

Here,  $v_k(t)$  represents the wavepacket profile for both filters, which has the same shape as the emitted photon envelopes [Fig. 3(c) in the main text] to enable the highest matching efficiency. The extracted modes fulfil bosonic commutation relations  $[\hat{a}_k, \hat{a}_k^\dagger] = 1$ , ensured by the normalization condition for the filter function  $\int_{-\infty}^{\infty} dt |f_k(t)|^2 = 1$ .

#### B. Denoising of moments

Due to measurement noise arising from cable losses, amplification chain, mode-matching inefficiency, and other factors, the directly obtained total mode from temporal template matching, denoted as  $\hat{S}_k$  ( $k = A, S$ ), does not solely

represent the target modes  $\hat{a}_k^{\text{out}}$ . Instead,  $\hat{S}_k$  comprises both the target mode  $\hat{a}_k^{\text{out}}$  and an additional noise mode  $\hat{h}^\dagger$ ,  $\hat{S}_k = \hat{a}_k^{\text{out}} + \hat{h}^\dagger$ . To remove the noise mode  $\hat{h}^\dagger$ , we operate an interleaved measurement, to sweep between two cases with and without both the parametric and second-order-transition drives. In the first case, we measure the total mode including both the targeted mode and the noise mode. In the second case, the target mode is left in vacuum and the measurement can be served as a reference of the noise mode. The switching between the two cases is repeated  $n = 5 \times 10^6$  times. We then calculate the averaged moments from these repetitions.

The first- and second-order moments of the two propagating modes,  $\langle \hat{a}_k^{\text{out}} \rangle$  and  $\langle (\hat{a}_k^{\text{out}})^\dagger \hat{a}_k^{\text{out}} \rangle$ , are obtained by [9]

$$\begin{aligned} \langle \hat{a}_k^{\text{out}} \rangle &= \langle \hat{S}_k - \hat{h}^\dagger \rangle, \\ \langle (\hat{a}_k^{\text{out}})^\dagger \hat{a}_k^{\text{out}} \rangle &= \langle \hat{S}_k^\dagger \hat{S}_k - \hat{S}_k \hat{h} - \hat{S}_k^\dagger \hat{h}^\dagger + \hat{h} \hat{h}^\dagger \rangle, \end{aligned} \quad (\text{S12})$$

where the angle brackets represent the averaging over the  $n$  repetitions. Generalized to fourth-order moments or more, the moments are computed as follows [9]:

$$\begin{aligned} \langle (\hat{S}_A^\dagger)^{m_A} \hat{S}_A^{n_A} (\hat{S}_S^\dagger)^{m_S} \hat{S}_S^{n_S} \rangle &= \sum_{i_A, j_A, i_S, j_S=0}^{m_A, n_A, m_S, n_S} \binom{m_A}{i_A} \binom{n_A}{j_A} \binom{m_S}{i_S} \binom{n_S}{j_S} \\ &\times \langle (\hat{a}_A^\dagger)^{i_A} \hat{a}_A^{j_A} (\hat{a}_S^\dagger)^{i_S} \hat{a}_S^{j_S} \rangle \langle (\hat{h}_A^\dagger)^{m_A - i_A} \hat{h}_A^{n_A - j_A} (\hat{h}_S^\dagger)^{m_S - i_S} \hat{h}_S^{n_S - j_S} \rangle. \end{aligned} \quad (\text{S13})$$

### C. Normalization of moments

The moments are normalized according to the assumption that, when the parametric drive or the second-order transition is turned on, the decay of qubit D occurs via two independent channels: the detected modes of the waveguide, and the intrinsic losses of qubit D, with rates  $\Gamma_{\text{eff}}$  and  $\Gamma_D$ , respectively. Accordingly, when qubit D is prepared in state  $|e\rangle$  or  $|f\rangle$  for photon emission in frequency  $\omega_A$  and  $\omega_S$ , respectively, we assume that the second-order moments are  $\langle \hat{a}_A^\dagger \hat{a}_A \rangle = \Gamma_{\text{eff}}^A / (\Gamma_{\text{eff}}^A + \Gamma_D^{ge})$  and  $\langle \hat{a}_S^\dagger \hat{a}_S \rangle = \Gamma_{\text{eff}}^S / (\Gamma_{\text{eff}}^S + \Gamma_D^{ef})$ , where  $\Gamma_{\text{eff}}^A / 2\pi = 4.59$  MHz and  $\Gamma_{\text{eff}}^S / 2\pi = 4.39$  MHz are the effective decay rate of the propagating modes obtained by exponentially fitting the emitted photon envelopes (Fig. S2).  $\Gamma_D^{ge}$  and  $\Gamma_D^{ef}$  are longitudinal relaxation rates of Qubit D, calculated as  $\Gamma_D^{ge} = 1/T'_{1,ge}$  and  $\Gamma_D^{ef} = 1/T'_{1,ef}$ .

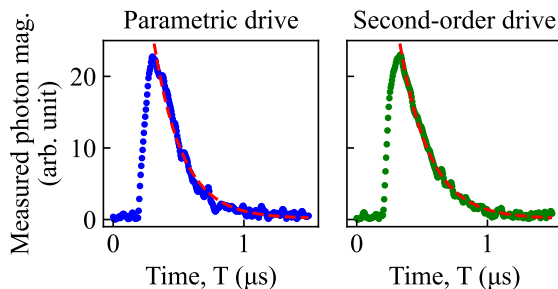


FIG. S2. Fitting of the emitter photon to obtain effective decay rate. The filled circles represent the measured photon magnitude, showing the same data as Fig. 3(c) in the main text. The dashed curves are the exponential fit.

### D. Joint quantum state tomography and process tomography

#### 1. least-squares method

In the joint quantum state tomography (QST) of the two propagating modes, we reconstruct the optimal density matrix from the first- to fourth-order moments of the two modes using least-squares (LS) optimization [10, 11]. Mathematically, the LS method solves the following convex optimization problem to find the optimal density matrix

$\rho$ :

$$\min_{\rho} \quad \left\| (\vec{\mathcal{B}} - \mathcal{A}\vec{\rho}) \right\|_{\ell_2}, \quad (\text{S14a})$$

$$\text{subject to} \quad \rho \geq 0, \quad (\text{S14b})$$

$$\text{Tr}(\rho) = 1, \quad (\text{S14c})$$

where  $\vec{\rho}$  in the objective function given in Eq. (S14a) represents the vectorized form of the density matrix. In Eq. (S14a),  $\vec{\mathcal{B}}$  is a column vector containing the experimentally measured first- to fourth-order moments,  $\langle (\hat{a}_A^\dagger)^{m_A} \hat{a}_A^{n_A} (\hat{a}_S^\dagger)^{m_S} \hat{a}_S^{n_S} \rangle$ , for  $m_A, n_A, m_S, n_S \in \{0, 1, 2\}$ . The matrix  $\mathcal{A}$ , commonly known as the sensing matrix [11], is determined solely by the operator basis set ( $\{|i\rangle\langle j|\}$ ) and the measurement observable set ( $\{(\hat{a}_A^\dagger)^{m_A} \hat{a}_A^{n_A} (\hat{a}_S^\dagger)^{m_S} \hat{a}_S^{n_S}\}$ ). Furthermore,  $\|\cdot\|_{\ell_2}$ , representing the  $\ell_2$  norm (also known as the Euclidean norm), is calculated as the square root of the sum of the squared components of a vector. The additional constraints given in Eq. (S14b-S14c) are completely positive (CP) and trace-preserving (TP) conditions of the density matrix, ensuring its physical validity. The convex optimization problem is solved using CVXPY [12].

To carry out quantum process tomography (QPT) of the state transfer scheme, we initialize Qubit D into four of the cardinal states,  $|g\rangle_D$ ,  $\frac{1}{\sqrt{2}}(|g\rangle_D + |e\rangle_D)$ ,  $|e\rangle_D$ , and  $\frac{1}{\sqrt{2}}(|g\rangle_D - i|e\rangle_D)$ . After the parametric drive and the second-order-transition drive, the state of Qubit D is transferred to the frequency-bin-encoded photonic modes. We then perform QST on the propagating modes followed by projection onto the space spanned by  $|1\rangle_{\omega_A} |0\rangle_{\omega_S}$  and  $|0\rangle_{\omega_A} |1\rangle_{\omega_S}$  for each initial state. Here we use the Kraus-operator formalism to represent the quantum process as [13]

$$\rho_{out} = \Lambda(\rho_{in}) = \sum_{m,n=0}^3 \chi_{mn} \sigma_m \rho_{in} \sigma_n^\dagger, \quad (\text{S15})$$

where  $\Lambda(\cdot)$  represents the quantum map; in our case, it is the state-transfer process from Qubit D to frequency-bin-encoded photonic modes. The quantities  $\chi_{mn}$  are elements of the process matrix  $\chi$  characterizing  $\Lambda$ . The  $\{\sigma_i\}$  are a fixed set of basis operators which are set to be Pauli operators,  $\{\sigma_0, \sigma_1, \sigma_2, \sigma_3\} = \{I, \sigma_x, \sigma_y, \sigma_z\}$ . Using Eq. (S15) with the four cardinal states (input probe states) and corresponding frequency-bin-encoded photon states (output states) we can form a system of linear equations of the form  $\mathcal{M}\vec{\chi} = \vec{\mathcal{D}}$ , where  $\vec{\mathcal{D}}$  is constructed from  $\rho_{out}$  and  $\vec{\chi}$  represents the vectorized form of the  $\chi$  matrix. The coefficient matrix  $\mathcal{M}$  [similar to the sensing matrix  $\mathcal{A}$  in Eq. (S14a)] depends only on the set of probe states and the measurement observables; in our case, the cardinal states and the moment operators. The recipe to reconstruct  $\mathcal{M}$  can be found in Ref. [14]. To calculate a physically valid  $\chi$  matrix characterizing an underlying CPTP map, we form a LS optimization problem (similar to QST) as follows,

$$\min_{\chi} \quad \left\| (\vec{\mathcal{D}} - \mathcal{M}\vec{\chi}) \right\|_{\ell_2}, \quad (\text{S16a})$$

$$\text{subject to} \quad \chi \geq 0, \quad (\text{S16b})$$

$$\sum_{m,n=0}^3 \chi_{mn} \sigma_m \sigma_n = I, \quad (\text{S16c})$$

where Eq. (S16b) and Eq. (S16c) ensure the CP and TP conditions respectively. Again, we use the CVXPY [12] tool to solve the convex optimization problem.

## 2. Gradient-descent method

In addition to LS optimization, we employ gradient-descent (GD) techniques with a rank-controlled ansatz for performing joint QST on frequency-bin-encoded photonic modes.

Here, the QST task is reformulated as a GD optimization problem utilizing Cholesky decomposition. The Cholesky decomposition of the density matrix is given as [15]

$$\rho(T) = \frac{T^\dagger T}{\text{Tr}(T^\dagger T)}, \quad (\text{S17})$$

where  $T$  is an  $r \times 4$ - dimensional arbitrary complex matrix, a rank-controlled ansatz. Here  $1 \leq r \leq 4$  acts as the rank of  $\rho(T)$ . The loss function to be minimized is:

$$\mathcal{L}[\rho(T)] = \sum_i \left| \mathcal{B}_i - \text{Tr} \left( \Pi_i \frac{T^\dagger T}{\text{Tr}(T^\dagger T)} \right) \right|^2, \quad (\text{S18})$$

where  $\{\Pi_i\}$  is the list of moment operators and  $\{\mathcal{B}_i\}$  is the list of experimentally measured moments. The goal of GD-QST is to find an optimal density matrix by iteratively minimizing the loss function  $\mathcal{L}[\rho(T)]$  according to the GD rule,

$$T_{i+1} = T_i - \lambda \nabla \mathcal{L}[\rho(T_i)], \quad (\text{S19})$$

where  $\nabla \mathcal{L}[\rho(T)]$  denotes the gradient of the loss function  $\mathcal{L}[\rho(T)]$  with respect to  $T$  at the  $i$ th step and the parameter  $\lambda$  represents the step size (usually referred to as the learning rate). The Cholesky parameterization always ensures the valid reconstruction of the density matrix at each iterative step. With a rank-1 ansatz ( $r = 1$ ), we enforce the reconstructed density matrix to be a pure state. This gives the best rank-1 approximation of the density matrix that fits the experimental data and minimizes the loss. This reconstruction effectively mitigates the noise and other incoherent errors, resulting in high state fidelity with the ideal pure state. As a result, the information encoded or transferred is recovered with high quality. Once the GD-QST is carried out (with rank-1 ansatz) on frequency-bin-encoded photonic modes, we then use reconstructed states to perform QPT and calculate the  $\chi$  matrix, which basically represents the unitary operation (since input and output states are pure states, the underlying operation is unitary). The rank-1 GD-QST method allows high-fidelity reconstruction of states and processes when the target states are pure and the process is unitary. The rank-4 GD-QST method yields results comparable to those obtained through LS optimization.

### 3. Detailed tomography results

From joint QST based on LS optimization, we obtain the density matrices of the two frequency-bin-encoded photonic modes, shown in Fig. 4(c-e) of the main text. Here, by tracing out one of the photonic states, we are left with the density matrices of two single modes in frequencies  $\omega_A$  and  $\omega_S$ , respectively [Fig. S3(a, b)].

In quantum process tomography, the four cardinal states are used for reconstructing the process matrix  $\chi$ , along with their corresponding fidelities, are presented in Table III. The second column lists the fidelities obtained from LS optimization. The first three states are depicted in the joint QST results [Fig. 4(c-e) in the main text], while the fourth state is an additional one necessary for QPT. The third column shows the fidelities achieved using GD-QST, with an average state fidelity of 97.7%. The close match between the reconstructed pure state and the ideal state indicates that we have little coherent error, and are limited by incoherent error. Additionally, the process fidelity of the identity operation turned out to be 98.5% (Fig. S4), showing a successful demonstration of the state-transfer scheme. Table III also provides the density matrices of these states from numerical simulations, which account for the coherence time of Qubit D.

TABLE III. The fidelity of the reconstructed density matrices for the four cardinal states are used in quantum process tomography, obtained from experimental measurements using LS and GD optimization, as well as from numerical simulations.

State	Measured fidelity from LS-QST	Measured fidelity from GD-QST	Simulated fidelity
$ 1\rangle_{\omega_A}  0\rangle_{\omega_S}$	89.97 %	98.13 %	95.52 %
$( 1\rangle_{\omega_A}  0\rangle_{\omega_S} +  0\rangle_{\omega_A}  1\rangle_{\omega_A})/\sqrt{2}$	87.14 %	97.26 %	95.16 %
$ 0\rangle_{\omega_A}  1\rangle_{\omega_A}$	83.14 %	96.25 %	95.09 %
$( 1\rangle_{\omega_A}  0\rangle_{\omega_S} - i  0\rangle_{\omega_A}  1\rangle_{\omega_A})/\sqrt{2}$	84.38 %	99.03 %	95.16 %

## IV. PROTOCOL OF QUANTUM STATE TRANSFER AND REMOTE ENTANGLEMENT

The frequency-bin-encoded photonic modes generated by our system have potential applications in quantum state transfer and establishing entanglement between two remote quantum processors, with the capability of detecting photon loss during transmission. While our experiment primarily demonstrates the generation of the frequency-bin photon, here we illustrate the complete process, which includes both the generation and the subsequent re-absorption of the photon by the receiving quantum processor.

The process of transferring quantum states between the emitter and receiver devices in our proposed frequency-bin-encoding-based distributed quantum computing system is shown in Fig. S5(a). As described in the main text, the emission of a frequency-bin-encoded photon begins by bringing the arbitrary superposition state  $\alpha |g\rangle + \beta |e\rangle$  on Qubit D into the state  $\alpha |e\rangle + \beta |f\rangle$  using  $\pi_{ef}$  and  $\pi_{ge}$  pulses. Following this, the parametric drive and second-order-transition drive are applied simultaneously to emit the two frequency-bin-encoded photonic modes. At the receiver

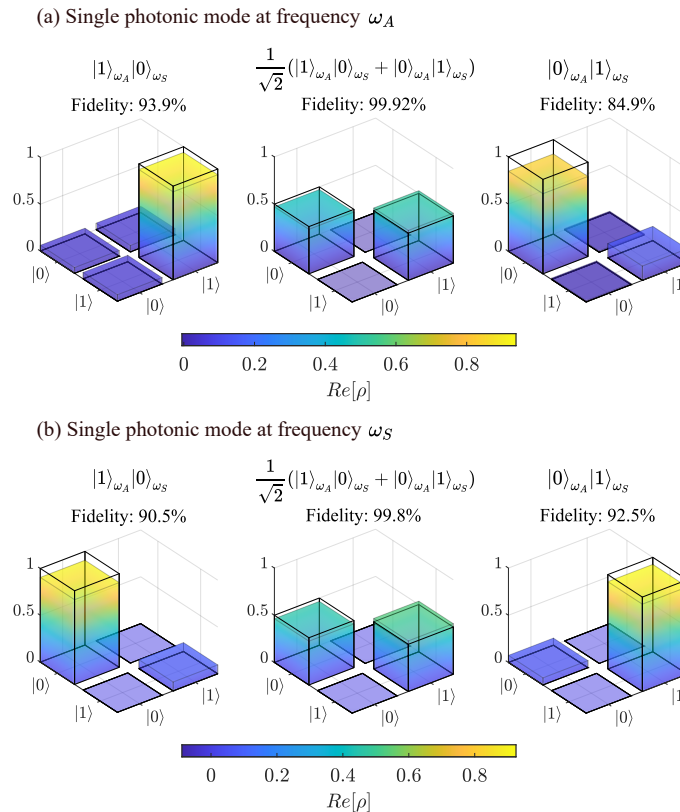


FIG. S3. The reconstructed (colored bars) and expected (black frames) density matrices of each frequency-bin-encoded photonic mode are shown, obtained by taking the partial trace of the two-mode density matrix, leaving only the single-mode density matrices at frequencies (a)  $\omega_A$  and (b)  $\omega_S$ , respectively. We present these matrices for three different initial states of Qubit D:  $|g\rangle_D$ ,  $\frac{1}{\sqrt{2}}(|g\rangle_D + |e\rangle_D)$ , and  $|e\rangle_D$ . The fidelity between the reconstructed and expected matrices is indicated above each corresponding matrix.

node, implemented with an identical quantum chip, the frequency-bin-encoded photonic modes are reabsorbed through the same process as the emission, but in reverse order. If any of the two frequency-bin photonic modes is lost before being absorbed, the state of Qubit D at the receiver will end up in the second excited state  $|f\rangle$  due to the last two  $\pi$ -pulses at the receiver. This is described in Table I in the main text.

The distributed quantum computing system facilitates the transfer of information between quantum processors. Typically, when using this system, the emitter and receiver nodes are coupled to extra quantum processors for computing large quantum tasks. To achieve entanglement between the qubits on the emitter and receiver devices, we can utilize the qubit in the quantum processor as an auxiliary qubit [Fig. S5(b)]. At the emitter node, an auxiliary qubit (denoted as X) from the quantum processor is coupled to the distributed quantum computing system. The entanglement between qubit X and qubit D is transferred to that between qubit D and the emitted frequency-bin-encoded photonic modes. At the receiver node, this establishes entanglement between qubit X at the emitter node and qubit D at the receiver node. Finally, if needed, a parametric drive is used to swap the state into another qubit X in the quantum processor at the receiver node, thereby entangling qubit X across both nodes. Similar to quantum state transfer, if the photon is lost before re-absorption, we can detect it since the qubit at the receiver will end up in the second excited state  $|f\rangle$ .

- 
- [1] C. Macklin, K. O'Brien, D. Hover, M. E. Schwartz, V. Bolkhovskiy, X. Zhang, W. D. Oliver, and I. Siddiqi, A near-quantum-limited Josephson traveling-wave parametric amplifier, *Science* **350**, 307 (2015).  
 [2] Intermodulation Product, *Vivace microwave platform*.  
 [3] S. E. Nigg, H. Paik, B. Vlastakis, G. Kirchmair, S. Shankar, L. Frunzio, M. Devoret, R. Schoelkopf, and S. Girvin, Black-box superconducting circuit quantization, *Physical Review Letters* **108**, 240502 (2012).



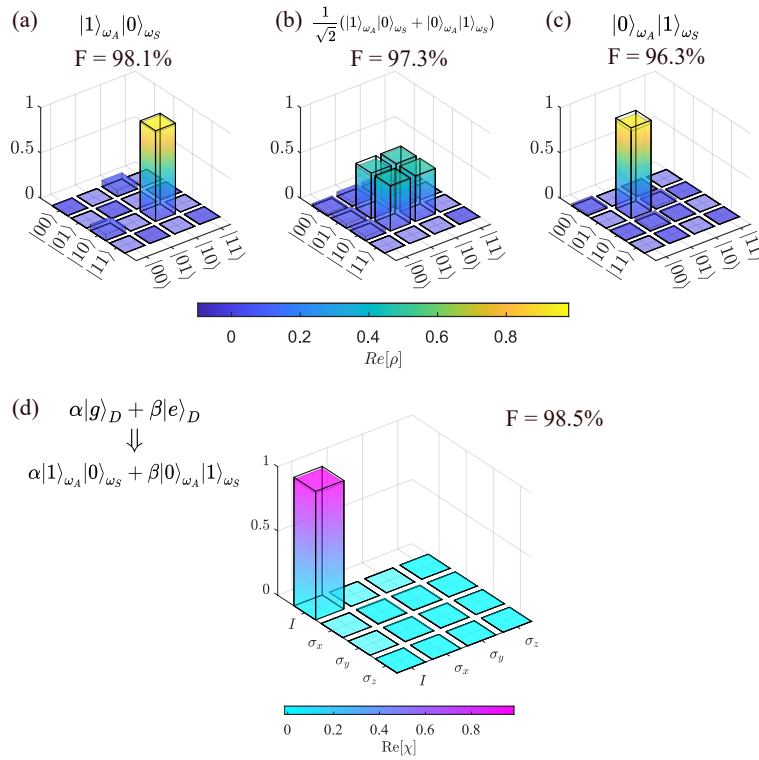


FIG. S4. Tomography of the frequency-bin-encoded photon output field, based on GD. (a-c) The reconstructed (colored bars) and expected (black wireframes) density matrices of the frequency-bin-encoded photonic modes for Qubit D initially in the states (b)  $|g\rangle_D$ , (c)  $\frac{1}{\sqrt{2}}(|g\rangle_D + |e\rangle_D)$ , and (d)  $|e\rangle_D$ . The fidelity  $F$  between the reconstructed and expected matrices is indicated above each corresponding density matrix. The imaginary components of the reconstructed density matrices are not shown; they are less than 0.1 across all elements of the matrices. (d) The  $\chi$  matrix for the data transfer between qubit D and the propagating mode, obtained from quantum process tomography measurements. The colored bars represent the measured results, while the black wireframes depict the ideal process. The imaginary components of the reconstructed  $\chi$  are not shown; they are less than 0.06 across all elements of the matrices.

- [4] M. Khanahmadi, M. M. Lund, K. Mølmer, and G. Johansson, Multimode character of quantum states released from a superconducting cavity, *Physical Review Research* **5**, 043071 (2023).
- [5] A. H. Küllerich and K. Mølmer, Input-output theory with quantum pulses, *Physical Review Letters* **123**, 123604 (2019).
- [6] H. J. Carmichael, Quantum trajectory theory for cascaded open systems, *Physical Review Letters* **70**, 2273 (1993).
- [7] R. Loudon, *The Quantum Theory of Light*, 3rd ed., Oxford Science Publications (Oxford University Press, Oxford ; New York, 2000).
- [8] C. W. Gardiner and P. Zoller, *Quantum Noise: A Handbook of Markovian and Non-Markovian Quantum Stochastic Methods with Applications to Quantum Optics*, 3rd ed., Springer Series in Synergetics (Springer, Berlin ; New York, 2004).
- [9] C. Eichler, Doctoral Thesis, ETH Zurich (2013).
- [10] R. Nehra, M. Eaton, C. González-Arciniegas, M. S. Kim, T. Gerrits, A. Lita, S. W. Nam, and O. Pfister, Generalized overlap quantum state tomography, *Physical Review Research* **2**, 042002 (2020).
- [11] I. Strandberg, Simple, reliable, and noise-resilient continuous-variable quantum state tomography with convex optimization, *Physical Review Applied* **18**, 044041 (2022).
- [12] S. Diamond and S. Boyd, CVXPY: A Python-embedded modeling language for convex optimization, *Journal of Machine Learning Research* **17**, 2909 (2016).
- [13] A. Gaikwad, K. Shende, Arvind, and K. Dorai, Implementing efficient selective quantum process tomography of superconducting quantum gates on ibm quantum experience, *Scientific Reports* **12**, 3688 (2022).
- [14] A. Gaikwad, Arvind, and K. Dorai, Efficient experimental characterization of quantum processes via compressed sensing on an nmr quantum processor, *Quantum Information Processing* **21**, 388 (2022).
- [15] Y. Wang, L. Liu, S. Cheng, L. Li, and J. Chen, Efficient factored gradient descent algorithm for quantum state tomography, *Physical Review Research* **6**, 033034 (2024).
- [16] C. A. Riofrío, D. Gross, S. T. Flammia, T. Monz, D. Nigg, R. Blatt, and J. Eisert, Experimental quantum compressed sensing for a seven-qubit system, *Nature Communications* **8**, 15305 (2017).

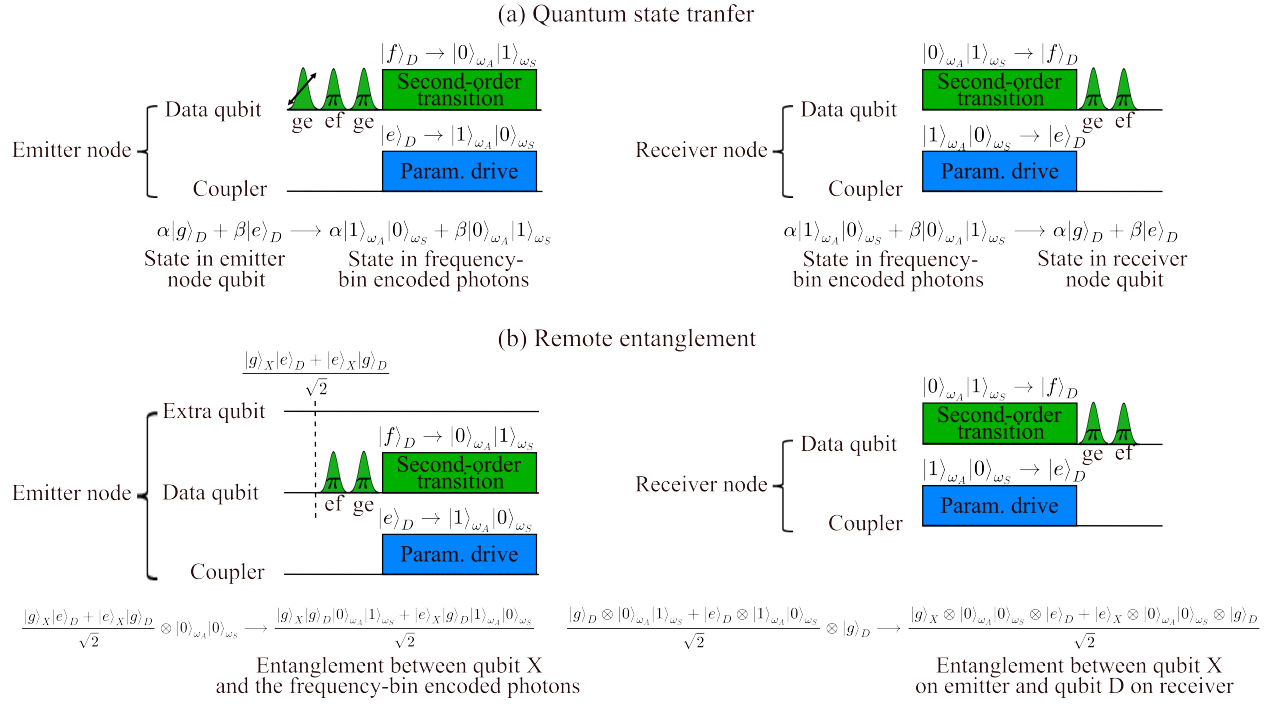


FIG. S5. The complete process of quantum state transfer and remote entanglement involves both the emitter and receiver nodes of the two quantum processors. In this work, we have experimentally implemented quantum state transfer at the emitter node. The remaining steps can be implemented similarly by simultaneously applying parametric and second-order-transition drives.